Artificial Water Channels Enable Fast and Selective Water Permeation Through Water-Wire Networks

Woochul Song[1,#], **Himanshu Joshi**[2], **Ratul Chowdhury**[1], **Joseph S. Najem**[3], **Yue-xiao Shen**[4], **Chao Lang**[1], **Codey B. Henderson**[5], **Yu-Ming Tu**[1,#], **Megan Farell**[1], **Megan E. Pitz**[3], **Costas D. Maranas**[1], **Paul S. Cremer**[5], **Robert J. Hickey**[6], **Stephen A. Sarles**[3], **Jun-li Hou**[7], **Aleksei Aksimentiev**[2], **Manish Kumar**[1,8,9,§,*]

[1]Department of Chemical Engineering, The Pennsylvania State University, University Park, PA 16802 USA

[2]Department of Physics, University of Illinois at Urbana-Champaign, Urbana, IL 61801 USA

[3]Department of Mechanical, Aerospace, and Biomedical Engineering, The University of Tennessee, Knoxville, TN 37996 USA

[4]Department of Chemistry, University of California, Berkeley, CA 94720 USA

[5]Department of Chemistry, The Pennsylvania State University, University Park, PA 16802 USA

[6]Department of Materials Science and Engineering, The Pennsylvania State University, University Park, PA 16802 USA

[7]Department of Chemistry, Fudan University, Shanghai, 200433 China

[8]Department of Biomedical Engineering, The Pennsylvania State University, University Park, PA 16802 USA

[9]Department of Civil and Environmental Engineering, The Pennsylvania State University, University Park, PA 16802 USA

Abstract

Artificial water channels are synthetic molecules that aim to mimic structural and functional features of biological water channels (aquaporins). Here, we report on a cluster-forming organic nanoarchitecture, peptide-appended hybrid[4]arene (PAH[4]), as a new class of artificial water channels. Fluorescence experiments and simulations demonstrated that PAH[4]s can form clusters

[*]Correspondence to: Manish Kumar, Tel.: 512-232-5838; manish.kumar@utexas.edu.
[#]Department of Chemical Engineering, The University of Texas at Austin, Austin, TX 78712 USA
[§]Department of Civil, Architectural and Environmental Engineering, The University of Texas at Austin, Austin, TX 78712 USA

in lipid membranes through lateral diffusion that provide synergistic membrane-spanning paths for rapid and selective water permeation through water-wire networks. Quantitative transport studies revealed that PAH[4]s can transport $>10^9$ water molecules per second per molecule, which is comparable to aquaporin water channels. The performance of these channels exceeds the upper bound limit of current desalination membranes by factor of ~10^4, as illustrated by the water/NaCl permeability-selectivity tradeoff curve. PAH[4]s' unique properties of high water/solute permselectivity via cooperative water wire formation could usher in an alternate design paradigm for permeable membrane materials in separations, energy production, and barrier applications.

Aquaporins (AQPs) are cellular membrane proteins that mediate translocation of water molecules across the physical membrane barrier at very high water permeation rates ($>10^9$ H_2O molecules per second per channel, $H_2O \cdot s^{-1} \cdot channel^{-1}$) with ultimate (theoretically infinite) water-to-ion selectivity, in order to maintain cellular homeostasis critical for maintaining life[1,2]. The unique structure and function of AQP-rich cell membranes, particularly its ideal water/salt permselectivity and spontaneous self-assembly and orientation in membrane matrices, are desirable features in desalination membranes[3,4]. Several attempts have been made to achieve successful integration of AQPs into practical desalination membranes[5]. However, challenges with preserving the integrity and translating the function of protein channels to larger scales during membrane fabrication processes have critically hampered researchers from achieving this goal[6].

As alternatives to biological water channels, bioinspired artificial water channels (AWCs) have rapidly emerged as a promising platform for next generation separation membranes[7,8]. AWCs are synthetic nanoarchitectures that mimic the function of AQPs. Insights from the wealth of structure-function relationships obtained from studies with AQPs have been used to suggest several biological channel traits as design criteria for AWCs including sub-nm unitary pore shape and a hydrophobic pore environment[7,9]. Recent success in AWC integration into scalable polymeric membranes have highlighted their possible advantages over AQPs in terms of stability and high pore packing density[10]. Achieving both AQP-like single channel water permeability and selectivity of AWCs, however, remains a challenge limiting the development of AWC-based desalination membranes[10–15].

We report on a new class of unimolecular transmembrane AWCs, peptide-appended hybrid[4]arenes (PAH[4]s), which exhibit $>10^9$ ($H_2O \cdot s^{-1} \cdot channel^{-1}$) water permeability that is comparable to AQPs (Fig. 1a–d). This transport was achieved through channel cluster formation within lipid bilayer membranes which provided cooperatively enhanced membrane-spanning water permeation paths (Fig. 1e–j). The structural design of PAH[4] originated from our attempts to synthesize AWCs with a pore size around ~3 Å (Supplementary Fig. 1), which is considered an ideal size for selective water permeation based on pore geometries of AQPs[16]. However, transport studies revealed that PAH[4]s mediated water conduction through entirely different mechanisms from traditional channel configurations that possess one (e.g., AQPs) or less than one (e.g., gramicidin A) vertical permeation path per channel molecule[17,18]. PAH[4]s conducted water through a previously unreported mechanism owing to unique structural and functional features (Fig. 1e,f).

Rapid water permeation via channel cluster formation

PAH[4]s were synthesized by attaching eight D-L-D phenylalanine tripeptides (triPhe) chains on hybrid[4]arene macrocycle molecules (Fig. 1a and Supplementary Fig. 1–4 and Supplementary Video 1). Hybrid[4]arenes were employed as building templates primarily due to their desirable narrowest internal cavity dimensions (~3 Å × ~5 Å) for selective water permeation (Supplementary Fig. 1). The dynamic structure of PAH[4] within lipid bilayers, however, provided multiple water permeation paths that were more preferred than a single permeation path vertically penetrating through each central cavity. As seen in the energy-minimized model of the PAH[4] molecule (Fig. 1d), triPhe chains are not rigidly held to each other by any specific interactions and form transient void windows facing outward with dimensions of around 5 – 7 Å, which are sterically and energetically more favorable for water permeation than the central pore cavity (Supplementary Fig. 5). This dynamic structure resulted in some interesting outcomes. When PAH[4]s clustered with each other within membranes, each void window could be interconnected with others from neighboring channels, providing cooperatively interconnected membrane-spanning paths for water permeation through water-wire networks (Fig. 1e–j).

We investigated water permeability of PAH[4]s in lipid bilayer membranes using stopped-flow light scattering experiments. PAH[4]s were reconstituted into phosphatidylcholine/phosphatidylserine (PC/PS) lipid vesicles (~200 nm diameter) with different molar ratios of channels to lipids (mCLRs) and the vesicles were exposed to outwardly directed osmotic pressure gradients (shrinking mode of vesicles). Water efflux from vesicles driven by osmotic pressure was evaluated by monitoring scattering intensity change of vesicles as was done in several recent studies (Supplementary Fig. 6)[9,12,13]. The rapid kinetics seen in scattering traces indicates a faster size change of vesicles with channel incorporation and, consequently, higher vesicular membrane permeability. Water permeability of lipid membranes increased with increasing mCLRs which indicated that embedded PAH[4]s enhanced membranes' water permeation rates (Fig. 2a and Supplementary Fig. 7). Single PAH[4] channel water permeability could be calculated by counting actual number of PAH[4]s per unit membrane area obtained from fluorescence correlation spectroscopy (FCS) measurements (Supplementary Fig. 8 and 9) at different mCLRs[9,10,12]. Interestingly, PAH[4]s exhibited enhanced single channel permeability at higher channel densities (> ~700 channels per μm^2 lipid membrane area) and the single channel permeability reached up to $3.7 \pm 0.3 \times 10^9$ $H_2O \cdot s^{-1} \cdot channel^{-1}$ or $1.1 \pm 0.1 \times 10^{-13}$ $cm^3 \cdot s^{-1} \cdot channel^{-1}$ at 25 °C (Fig. 2b), the highest among the reported values of AWCs except for carbon nanotube porins of ~8 Å diameter (CNTPs). These values are even comparable to that of AQP1s (4.0×10^9 $H_2O \cdot s^{-1} \cdot channel^{-1}$) (Fig. 2c). While we exploited most the widely adapted model to calculate water permeability of PAH[4] channel to maintain consistency of evaluating PAH[4] channels with published references, Pohl and coworkers have recently proposed a more accurate equation to quantify water permeability[9,19]. When this model was used for PAH[4]s, the single channel permeability was calculated to be slightly lower at $8.9 \pm 0.8 \times 10^8$ $H_2O \cdot s^{-1} \cdot channel^{-1}$ (see Supplementary Information for details). It has been reported previously that the permeability of a specific AWC, peptide-appended pillar[5]arene (PAP[5]), was different in liposomes based on whether permeability was measured in the

swelling or the shrinkage mode[12]. However, only a small permeability enhancement (1.3 – 2.5 times) was observed for PAH[4] channels when measured in the swelling mode (Supplementary Fig. 10). It has also been reported that chaotropic osmolytes such as poly(ethylene glycol) (PEG) could disrupt intermolecular H-bonds between water molecules and enhance water permeation rate through CNTPs, but this effect of osmolytes was not observed in the case of PAH[4] channels (Supplementary Fig. 11).

PAH[4] clusters in lipid bilayer membranes were observed by atomic force microscopy (AFM) performed in an aqueous buffer (Fig. 1h) and the domain size of channel clusters observed from AFM experiments match well with the number of PAH[4] subunits per vesicle estimated by FCS (Supplementary Fig. 12). Further, PAH[4]s' cluster-forming behavior in lipid bilayer membranes was confirmed via fluorescence recovery after photobleaching (FRAP) experiments (Supplementary Fig. 13) and molecular dynamics (MD) simulations (Fig. 1g). These results are similar to our recent study that demonstrated aggregation behavior of another triPhe chain based unimolecular AWC, PAP[5][10,12]. Combined with the increased single channel permeability observed with increasing channel densities at the low membrane concentration range (Fig. 2b), these results indicate cooperatively enhanced water permeation via channel cluster formation.

Measured single channel permeability indicated that PAH[4]s can mediate water transport as efficiently as AQP1. This was further confirmed by measurement of activation energy of water permeation through the channels (Fig. 2d and Supplementary Fig. 14). Control lipid membranes were shown to have the activation energy of 11.1 ± 0.8 kcal/mol for water permeation, which corresponds to reported reference values of lipid bilayers where water permeation takes place through the solution-diffusion mechanism[20,21]. The activation energy for PAH[4]-mediated water permeation was measured as 3.6 ± 1.2 kcal/mol, indicating a lower energy barrier for water permeation across the membranes by PAH[4] insertion. This low activation energy (< 5 kcal/mol) is strong evidence of single-file water transport[22]. Based on the measured activation energy and presumption of single file water conduction, permeability was calculated as 6.9×10^{-13} cm^3·channel^{-1}, which is in good agreement with measured single PAH[4] permeability (see Supplementary Information for calculation details). This confirms single file water permeation through PAH[4] architectures across the membranes[22], which is also validated by our MD simulation results.

Quantitative measurement of monovalent ion permeability

As mentioned earlier, achieving both high permeability and selectivity is a significant challenge for membrane systems in general and AWC systems in particular—the other challenge is methodological. The water over ion selectivity properties of all AWCs reported so far have been obtained using qualitative techniques rather than numerical values such as number ratios between permeating water and ion molecules which represent intrinsic molecular transport properties[15,23]. This challenge has also been recently discussed for desalination membranes and, in order to provide a baseline for membrane material development efforts, Park and coworkers reported an upper bound plot of intrinsic water/NaCl permeability-selectivity tradeoff for representative polymeric desalination membranes[24]. We propose that obtaining channels' intrinsic transport properties is quite

important to achieve coherence in terms of evaluating AWCs for any future applications including desalination.

A combination of colloidal quenching halide ion sensitive dyes (lucigenin dyes), stopped-flow fluorescence spectrometry, and FCS techniques were exploited to evaluate quantitative PAH[4] channel chloride (Cl^-) permeability (see Supplementary Information for analysis details) (Fig. 2e,f and Supplementary Fig. 15). Cl^- ion fluxes were measured at different Cl^- concentration gradients for both control and PAH[4]-reconstituted membranes (Fig. 2f and Supplementary Fig. 16) and Cl^- permeability coefficient of lipid membranes was measured as 8.6 (± 1.9) $\times 10^{-10}$ cm/s which corresponds to reported Cl^- permeability coefficients of lipid bilayers (10^{-8} - 10^{-11} cm/s)[25]. Single PAH[4] Cl^- permeability was calculated using channel numbers per membrane area obtained from FCS analysis to be 9.5 (± 3.6) $\times 10^{-23}$ cm^3/s. Channel area (~2 nm^2) normalized Cl^- permeability coefficient was 4.7 (± 1.7) $\times 10^{-9}$ cm/s, which is ~5 folds higher than highly retentive lipid membranes. When combined with water permeability ($3.6 \pm 0.3 \times 10^9$ $H_2O \cdot s^{-1} \cdot channel^{-1}$ or 1.1 (± 0.1) $\times 10^{-13}$ cm^3/s), PAH[4] exhibits a ~10^9 water/salt selectivity that far surpasses selectivity requirements (~16,000) for desalination membranes[3].

Absence of suitably sensitive cation colloidal quenching dyes makes it difficult to measure single channel Na^+ permeability. Alternatively, 8-hydroxypyrene-1,3,6-trisulfonic acid (HPTS) dye based assay was performed to observe if any effective Na^+ permeation occurs through PAH[4]s as this method has been widely adopted for testing ion permeation through various ion channels[26], but no detectable Na^+ permeation was observed for PAH[4]-reconstituted membranes (Supplementary Fig. 17).

Ionic current measurements across PAH[4] reconstituted lipid bilayers were performed to demonstrate the highly retentive ion permeation properties of PAH[4]s, using a droplet interface bilayer (DIB) system[27,28]. The DIB system exploits PAH[4] reconstituted PC/PC vesicles, which were confirmed to have PAH[4]s embedded in membranes from stopped-flow experiments, to form bilayers at the interface of two droplets and, thereby, maximize the opportunity of PAH[4] presence in DIB membranes during the ionic current measurements (Fig. 2g and Supplementary Fig. 18). During the course of current-to-voltage (I-V) measurements, PAH[4]-reconstituted membranes did not show any ionic current at any tested conditions and the resistance value of the membranes (~5 GΩ) was equivalent to control insulating lipid bilayer membranes[27,29–31], demonstrating the highly efficient ionic rejection of PAH[4]s (Fig. 2h). In terms of interpretation of this result, it is still possible that PAH[4]s were not successfully integrated into the membranes during the DIB formation process (Supplementary Fig. 18). Therefore, unimolecular AWC PAP[5], which is structurally analogous to PAH[4] (Supplementary Fig. 2) and known to allow ion permeation in our previous study[12], was used as a positive control and subjected to I-V measurements using DIB system to show stable insertion of triPhe chain based unimolecular transmembrane structures into the membranes, during the DIB formation. Under the same conditions, PAP[5] reconstituted membranes showed significant ionic currents with lowered membrane resistance values of ~5 – 13 MΩ (Fig. 2i).

Evaluation of PAH[4] channel water-to-salt permselectivity

Based on experimentally measured molecular transport rates, PAH[4]s' intrinsic permeability of water (P_w) and salt (NaCl, P_s) were calculated as $2.2 \pm 0.2 \times 10^{-6}$ cm^2/s and $1.9 \pm 0.7 \times 10^{-15}$ cm^2/s, respectively (see Supplementary Information for analysis details) using chloride as the limiting ion. Note that, instead of pore area, cross-sectional channel area (~2 nm^2) occupied in membranes was used to calculate individual permeability values to provide a membrane engineering perspective[32]. Since water channel integration efficiency into biomimetic membrane matrix is another critical factor in evaluating channel-based membranes, PAH[4]-reconstituted PC/PS lipid membranes' P_w and P_s values were calculated for several cases of channel integration efficiency (α) ranging from 0.01 to 1, and compared to reported desalination membranes' values (Fig. 3). Additionally, representative biomimetic water channels (CNTPs and *Rhodobacter sphaeroides* aquaporin Z (RsAqpZ) that is reported to have the highest permeability among the AQP family[33]) based membranes were plotted using same method to provide a comparison of the various types of channel based biomimetic membranes possible for desalination membrane development. As shown in Fig. 3, plotting water/salt selectivity (P_w/P_s) against water permeability (P_w) shows that PC/PS lipid membrane matrices by themselves are below the tradeoff upper limit of polymeric desalination membranes. This is reasonable, given that water and salt permeations take place via the solution-diffusion mechanism for both cases. Remarkably, upon gradual increase in channel insertion into membranes ($\alpha = 0.01 \sim 1$), channel-based biomimetic membranes demonstrate water/NaCl selectivity far exceeding state-of-the-art polymeric membranes' upper bound limit by several orders of magnitude (Fig. 3). We propose that this is a conservative estimate of the permeability selectivity trend for PAH[4]-enhanced biomimetic matrices because we used quantitative Cl$^-$ ion permeability as a model for NaCl permeability. Usually, under reverse-osmosis conditions, Cl$^-$ permeation is limited by slower diffusing Na$^+$. This assumption of Na$^+$ being the limiting ion has been used recently to estimate, based on indirect measurements, that biomimetic membranes could have NaCl selectivity in a range three orders of magnitude higher than shown here[32]. Hence, values reported here represent the most conservative evaluation of PAH[4] channel-based desalination membranes with direct measurements of channel transport rates. However, it is possible that PAH[4] channels could demonstrate ~10^{12} water to salt selectivity as estimated in the previous study for AQPs[32] if Na$^+$ ion transport rates could be measured accurately and used instead.

Computer simulations of PAH[4] permeability

To provide detailed descriptions relating microstructure-to-molecular transport properties of PAH[4] clusters, representative PAH[4] cluster configurations were generated *in silico* and subjected to MD simulations (~400 ns) in lipid bilayer patches (see Supplementary Information for detailed simulation analysis) (Fig. 4a,b and Supplementary Video 2). As PAH[4] configurations evolved from monomer to dimer and to 22-mer clusters, water permeability per PAH[4] molecule enhanced significantly suggesting cooperative water permeating path formation between PAH[4] molecules (Supplementary Fig. 19–26). The agreement in permeability values between experimental and simulation while recapitulating the experimental trend of increasing permeability when clusters are formed with increasing

channel density, represents the appropriateness of the simulation setting to emulate oligomerized PAH[4] clusters in lipid membranes. In another set of simulations, a transmembrane voltage of +/− 1 V was applied in two MD simulation of the most water conductive PAH[4] 22-mer clusters to measure ionic conductance, but no ion permeation was observed during each 100 ns simulation, confirming the ion exclusion property of PAH[4] channels (Supplementary Video 3). In term of a numerical value these simulations indicate that the conductance of the membrane patch was <1 pS.

Full MD trajectories provided several insights into rapid water permeation through PAH[4] clusters. First, all permeating water molecules have to undergo at least one "bulk – 2D wire – bulk" transition. 2D water wire formation is a crucial factor of enabling rapid water conduction via almost perfect slippage of water molecules, which cannot be achieved in the systems where continuum hydrodynamics is predominant[34]. Water wire formation is not seen in monomeric PAH[4] configurations supporting the assertion that PAH[4]s provide synergistic paths via cluster formation (Supplementary Fig. 27). Specifically, analyses of the number of H-bonds for each of ~800 water molecules that permeated through the PAH[4] 22-mer cluster showed several interesting features in comparison to that in an AQP1 tetramer. As a water molecule approaches the center of the membrane, the number of H-bonds that it forms gradually reduces from an average of ~3.5 to ~2.5 on both sides of the membrane and then drops rapidly to ~1.5 within the constriction region of the channel, at Z-axis values within 9 Å from the membrane's midplane (Fig. 4c); the number of H-bonds lower than two in the constriction region indicates that water molecules loss its bulk state enabling fast permeation in this region[13]. A similar dependence was observed for AQP1 with one major difference: the location of the minimally H-bonded water molecule was well-defined by the channel's structure while this location was not well defined in the dynamic PAH[4] clusters. Further, the varying numbers of H-bonds formed by ten randomly chosen water molecules as they pass through each channel was plotted (Supplementary Fig. 28) for both PAH[4] and AQP1 channels. This analysis indicated that, in the case of the PAH[4] cluster system, the number of H-bonds of each water molecule could drop even lower than 1.5 during individual permeation events similar to that in AQP1 (Supplementary Fig. 28). However, due to the lack of a well-defined structure for PAH[4] clusters, averaging over all permeating molecule produces a slightly higher minimum number of H-bonds in the constriction region for PAH[4] as compared to AQP1.

We used the obtained dependence of the number of H-bonds along the Z axis to define the average location of the channel constriction region for both PAH[4] and AQP1 systems: [−9 Å, 9 Å] and [−14 Å, 14 Å], respectively. Having defined the boundaries of the channel constriction, we determined the path each water molecule took to permeate the PAH[4] cluster or the AQP1 tetramer (two such paths are shown for each system in Fig. 4d,e) and computed the time it took for each water molecule to pass from one side of the constriction to the other for the both systems (Supplementary Fig. 29). The histograms of normalized probability of the permeation times are shown in Fig. 4f and g for PAH[4] and AQP1, respectively. As expected, the histogram has a longer tail in the case of the PAH[4] 22-mer cluster, reflective of the more convoluted permeation path for some water molecules. The average permeation time is, however, of the same order: 20.3 ns for PAH[4] and 5.5 ns for AQP1, with the AQP1 channel showing a four-fold faster transport per permeation path.

We further computed the average distance travelled by a water molecule (Supplementary Fig. 30). The average permeation path is slightly longer for the PAH[4] channel than for AQP1 as can be seen from the normalized distributions of the water permeation path lengths (Fig. 4h,i). We have used the average location of the water molecules in 1Å Z-axis bins to visualize a typical permeation path through PAH[4] cluster and AQP1 (Fig. 4d,e). In the case of AQP1, the permeation path is well defined, whereas for PAH[4] the path can be either well-defined or dispersed. The results of our analysis suggest that both the average time and the average path taken by a water molecule permeating through an PAH[4] cluster is of the same order as that for the APQ1 channel. While both permeation time and permeation path are statistically longer for PAH[4], the overall permeation rate can approach that of AQP1 if a sufficient number of such channels simultaneously forms per unit area of the membrane, providing highly efficient water permeation networks (Supplementary Videos 4 and 5). This conclusion is also supported by corresponding experimental observations (channel aggregation and increasing channel permeability at higher channel densities).

Summary

The transmembrane unimolecular PAH[4] architecture was shown to enable highly efficient and selective water permeation through mechanisms distinct from traditional water channels. These mechanisms include lateral aggregation and interconnected water wire network formation in a biomimetic membrane matrix which results in intrinsic water/NaCl transport properties that exceeds current desalination membranes permselectivity performance by orders of magnitude. Combined with recent progress in maximizing AWC insertion efficiency in bioinspired block copolymer membranes by up to ~60 % and utilizing them for fabrication of scalable membranes[10], cluster-forming AWCs could pave the way for a unique architecture of bioinspired membranes for a variety of applications.

Methods

PAH[4] reconstitution into lipid vesicles.

Both control lipid and PAH[4]-reconstituted lipid vesicular membranes were prepared by the film rehydration method[35]. 3 mg total of phosphatidylcholine (PC) and phosphatidylserine (PS) lipid mixture with molar ratio of 4:1 (mol/mol) was dissolved in chloroform ($CHCl_3$). Needed amounts of PAH[4]s depending on desired molar ratios of channels to lipids (mCLRs) were calculated and dissolved in lipid chloroform solutions. The solutions were transferred into 50 ml round bottomed flasks and gently dried using a rotary evaporator to form lipid films on the bottom of flasks. Any residual solvent ($CHCl_3$) was removed by placing the flasks in a high vacuum chamber for 16 hours. Completely dried films were rehydrated with 1 ml of rehydration buffer (10 mM HEPES, 100 mM NaCl, and 0.01% (w/v) NaN_3 at pH 7.0) and extruded 15 times through 0.2 μm polycarbonate track-etched membranes to obtain uniformly sized lipid vesicles with ~200 nm diameter, which were confirmed by Zetasizer Nano-ZS90 (Malvern Panalytical).

Water permeability measurement of vesicular membranes.

Water permeability (P_f, m·s^{-1}) of lipid vesicular membranes were measured using SF-300X stopped-flow instrument (KinTek). Vesicles were abruptly exposed to hypertonic solution (10 mM HEPES, 100 mM NaCl, 100 mM PEG$_{600}$, and 0.01% (w/v) NaN$_3$ at pH 7.0) by mixing in the stopped flow cell in order to impose an outwardly directed osmotic pressure across the vesicular membranes, and the membrane permeabilities were calculated based on the amount of water efflux from the vesicles driven by the osmotic gradient (shrinking mode of vesicles) (Supplementary Fig. 6). Size change of vesicles due to water efflux was monitored through side-scattering (detection angle of 90° against to incident light of 600 nm wavelength) intensity change with less than 10 milliseconds of dead-time after mixing, in order to obtain accurate kinetic information[36]. Kinetic coefficients (k) of size change of vesicles were obtained by fitting scattering traces into double-exponential functions and used to calculate osmotic permeability (P_f, m·s^{-1}) of vesicular membranes (Supplementary Fig. 7), using the following equation (1)[20].

$$P_f\left(m \cdot s^{-1}\right) = \frac{k}{(S/V_0) \times v_w \times \Delta C_{osm}}$$

(1)

where k is a larger exponential coefficient of fitted double-exponential function, S is initial surface area of vesicles, V_0 is initial volume of vesicles, v_w is the molar volume of water, and $_{osmol}$ is imposed difference of osmolarity across vesicular membranes. Note that, for single channel permeability measurements from mCLR 0.00001 vesicles, smaller exponential coefficient (k) of fitted double-exponential function was used, because no apparent permeability increase was seen between control vesicles and mCLR 0.00001 vesicles from the first exponent. This approach was previously demonstrated and used to characterize water channels that have low water permeability[12,37]. Accurate C_{osm} values were measured using a freezing point osmometer (Model 3300, Advanced Instruments) for all tested solutions.

FCS for evaluating single PAH[4] channel water permeability.

To calculate single PAH[4] channel permeability, actual number of PAH[4]s embedded in reconstituted lipid vesicles was counted using fluorescence correlation spectroscopy (FCS). For FCS analysis, PAH[4]s were first labeled with (5-(and-6)-((N-(5-aminopentyl)amino)carbonyl)tetramethylrhodamine) (Invitrogen) dyes using dicyclohexylcarbodiimide (DCC) chemical cross linkers (Thermo Fisher Scientific). Molar ratio of 1:8:8 of PAH[4]s, dyes, and DCCs were dissolved in dimethyl sulfoxide (DMSO) and reacted for 16 hours by stirring at room temperature. Unreacted dyes were removed via dialysis using Slide-A-Lyzer™ MINI device (Thermo Fisher Scientific) for five days, changing fresh DMSO every 12 hours. After free dye removal by dialysis, labeled PAH[4] channels were harvested by fully evaporating DMSO solvent inside high vacuum chamber for two days, and used for both FCS and fluorescence recovery after photobleaching (FRAP) experiments. Dye-labeled PAH[4]s were reconstituted into lipid vesicles using film rehydration method and the reconstituted vesicles were subsequently subjected to FCS analysis. Fluorescence intensity fluctuation of vesicles ($\delta F(t)$) in a small confocal volume was monitored using a confocal microscope equipped with a time-resolved single-photon

counting module (Becker-Hickl GmbH) and autocorrelation function ($G(t)$) was obtained based on following equation (2).

$$G(\tau) = \frac{\langle \delta F(t) \rangle \langle \delta F(t + \tau) \rangle}{\langle F(t) \rangle^2} \tag{2}$$

where t is time and τ is time lag. $G(\tau)$ is specifically related with several parameters as equation (3).

$$G(\tau) = \frac{1}{N} \sum_{i=1}^{M} f_i \left[\frac{1}{1 + \tau/\tau_{D_i}} \right] \left[\frac{1}{1 + (r/z)^2 \left(\tau/\tau_{D_i} \right)} \right]^{1/2} \tag{3}$$

where r and z are radius and half height of confocal volume, τ_{D_i} is lateral diffusion time of fluorescence species i, and N is total number of fluorescent species in a confocal volume which is the number of reconstituted vesicles (N_{ves}) in this case. N_{ves} could be simply obtained from y-axis intercept of autocorrelation function ($G(0) = 1/N_{ves}$). After that, vesicles were completely micellized by adding 10 % (w/v) of nonionic detergent octyl-β, D-glucoside (OG) and the number of channels (N_{chan}) were obtained using same procedure of obtaining N_{ves} (Supplementary Fig. 8 and 9). Average number of channels per vesicles (N_{chan}/N_{ves}) was used to calculate both channel densities in lipid membranes and single channel PAH[4] permeability.

Atomic force microscopy (AFM) imaging of PAH[4] clusters in supported bilayer membranes.

AFM analyses were performed to observe PAH[4] channel clusters in lipid bilayer membranes. Control and PAH[4]-reconstituted (mCLR 0.005) PC/PS vesicles were prepared as described above with additional buffer composition of 3mM $CaCl_2$. Supported bilayer membranes were prepared by rupturing vesicles (suspending diluted vesicle solutions) on freshly cleaved mica. After 1.5 hours of incubation time, membranes were gently washed with water and subjected to AFM imaging in liquid (water) on a Bruker BioScope Resolve AFM. These liquid AFM measurements were conducted in PeakForce tapping mode using a ScanAsyst Fluid+ tip with a spring constant of 0.7 N/m. The force used for both the control and PAH[4] channel samples was 750 pN or less, and the images contained a minimum of 384 pixels per line. The acquired images were plane-fit to the first order to account for sample tilt. Multiple line scans were utilized throughout the scan containing PAH[4] channels to determine the size of their domains. For PAH[4]-reconstituted membranes, island domains with ~30 nm diameters (in adhesion mode) were identified spreading over the entire membrane which was not seen in control lipid membranes (Supplementary Fig. 12).

FRAP analysis to observe lateral diffusion of PAH[4]s in lipid bilayer membranes.

Two PC/PS vesicles were prepared; one is PC/PS vesicles with dye-labeled PAH[4]s (mCLR 0.005) and the other (control vesicle) is PC/PS with PAH[4]s (unlabeled, mCLR 0.005) and additional 0.5 mol% of Texas Red 1,2-Dihexadecanoly-sn-Glycero-e-Phosphoethanolamine

(TR-DHPE) lipids. TR-DHPE containing control vesicles were used to confirm bilayer formation and obtain membrane viscosity as described later. The vesicle solutions were combined with a buffer solution to create a vesicle environment with a final concentration of 2 mM CaCl$_2$, 100 mM NaCl, and 10 mM HEPES at pH 7. Supported bilayers were made by rupturing vesicles on a cleaned glass coverslip in a polydimethylsiloxane (PDMS) well. After a fusion time of 10 minutes, the formed bilayers were rinsed with buffer (100 mM NaCl, 10 mM HEPES at pH 7.0), scratched with tweezers to remove a small section of bilayer, and rinsing with the same buffer a second time. The FRAP experiments were conducted on a Nikon Eclipse TE-2000-U inverted microscope through a 10X objective lens. A 532 nm laser (Spectra Physics) was used to bleach the labeled channel or the TR-DHPE. The bleach spot diameter was approximately 16 μm. Fluorescence intensity was monitored every three seconds for the initial 75 seconds, then every 30 seconds for the remainder of the experiments (Supplementary Fig. 13). The fluorescent recovery curves were used to determine the diffusion coefficients of the labeled PAH[4] channel and TR-DHPE, respectively. The fluorescence intensity of the bleached spot at a given time was divided by the intensity of a non-bleached region to correct for differences in light intensity and photobleaching. The normalized fluorescence recovery, $f(t)$, was calculated using the following equation (4).

$$f(t) = \frac{I_t - I_0}{I_i - I_0} \tag{4}$$

where I_t is the normalized spot intensity at time t, I_0 is the normalized spot intensity immediately following bleaching, and I_i is the average spot intensity prior to bleaching.

The recovery as a function of time was fit to an exponential equation to obtain the mobile fraction, A, as well as the time of half recovery, $\tau_{1/2}$, shown in equation (5) and (6).

$$f(t) = A\left(1 - e^{-\tau t}\right). \tag{5}$$

$$\tau_{1/2} = \frac{\ln 2}{\tau}. \tag{6}$$

The lateral diffusion coefficient, D_{lat}, was calculated as follows, where ω is the half-width of the Gaussian laser beam (7).

$$D_{lat} = \frac{0.88 \times \omega^2}{4 \times \tau_{1/2}}. \tag{7}$$

Measurement of activation energy of water permeation through PAH[4] channels.

Water permeability measurements of both control and channel-reconstituted lipid membranes were repeated at different temperatures (between 5 and 25 °C), in order to measure activation energy (E_a) of water permeation through channels as well as lipid

membrane matrix (Supplementary Fig. 14). Measurements were performed under the swelling mode for this part of the study. Channel-mediated water permeabilities at each temperature were obtained by subtracting control lipid membranes' permeability from channel-reconstituted membranes' permeability. Water permeability (P_f, μm·s^{-1}) and E_a of water permeation is related by the Arrhenius equation (8)[13,21,22].

$$P_f\left(\mu m \cdot s^{-1}\right) = Ae^{\frac{-E_a}{RT}} \tag{8}$$

where A is pre-exponential constant, R is ideal gas constant, and T is temperature (K). E_a can be simply extracted from a slope of the Arrhenius plot as shown in equation (9) (Fig. 2d).

$$\ln P_f\left(\mu m \cdot s^{-1}\right) = \ln A - \frac{E_a}{R}\frac{1}{T} \tag{9}$$

Cl$^-$ ion permeability measurement.

Measurements of Cl$^-$ permeability of both control and PAH[4]-reconstituted lipid vesicular membranes were performed using stopped-flow fluorescence experiments. Among several halide ion sensitive colloidal quenching dyes, lucigenin dyes were selected as measurement probes due to their highest Stern-Volmer constant value among commercial dyes (K_{sv} = 390 M^{-1} for chloride ions in aqueous solutions) and, therefore, highest sensitivity to Cl$^-$ concentration change[38]. To measure accurate Cl$^-$ influx into vesicular membranes, the K_{sv} of lucigenin inside ~200 nm PC/PS vesicles was first determined (95 M^{-1} for intravesicular environments, Supplementary Fig. 15). Excitation wavelength was set as 455 nm using a monochromator and PMT module was equipped with BrightLine® fluorescence 534/30 emission filter. Lucigenin-encapsulating vesicles prepared with Cl$^-$ free buffer (10 mM HEPES, 100 mM KNO$_3$, 10 μM valinomycin and 0.01% (w/v) NaN$_3$ at pH 7.0) were abruptly exposed to different Cl$^-$ gradients in the stopped-flow measurement cell (e.g., in order to impose 20 mM Cl$^-$ gradient, same volumetric amount of Cl$^-$ containing buffer (10 mM HEPES, 40 mM KCl, 60 mM KNO$_3$, 10 μM valinomycin and 0.01% (w/v) NaN$_3$ at pH 7.0) to vesicle solution was mixed in the measurement cell), and fluorescence intensity change was monitored. Note that potassium ionophore valinomycin was added to the vesicles beforehand to mitigate charge imbalance across the membrane, and therefore prevent underestimation of Cl$^-$ permeability due to electrical potential developed as a consequence. Initial fluorescence kinetic information ($dF/dt|_{t=0}$) is quite important for accurate evaluation of Cl$^-$ permeability and stopped-flow traces (Supplementary Fig. 16). More than 10 traces of fluorescence intensity change were recorded for each measurement and the averaged trace was used for analysis. Vesicular membranes' mole flux of Cl$^-$ ion (j_{Cl}) at each tested Cl$^-$ concentration condition was calculated by equation (10).

$$j_{Cl} = \frac{d(mole)}{S \times dt} = \frac{V}{S}\frac{d[Cl^-]}{dt}\bigg|_{t=0} = \frac{-V}{S \times K_{sv} \times F_0}\frac{dF}{dt}\bigg|_{t=0} \tag{10}$$

where S and V are surface area and volume of vesicles, $[cl^-]$ is molar concentration of Cl^- ions inside vesicles, K_{sv} is the determined Stern-Volmer constant of lucigenin dyes inside vesicles ($\sim$95 M^{-1}), F_0 is fluorescence intensity under Cl^- free condition (fluorescence intensity at t = 0). Cl^- permeability coefficient (B_{Cl}, $cm \cdot s^{-1}$) of membranes was obtained from slope of j_{Cl} plot as a function of Cl^- concentration gradients (11) (Fig. 2f).

$$B_{Cl} = \frac{dj_{Cl}}{d[Cl^-]} \tag{11}$$

Single PAH[4] channel Cl^- permeability coefficient ($B_{Cl,PAH}$, $cm^3 \cdot s^{-1}$) was calculated based on channel density in lipid membranes obtained from FCS analyses (12).

$$B_{Cl,PAH} = \frac{d(j_{Cl,PAH,lipid} - j_{Cl,lipid})}{d[Cl^-]} \times \frac{1}{\sigma_{PAH}} \tag{12}$$

where $j_{Cl,PAH,lipid}$ is PAH-reconstituted membranes' Cl^- mole flux, $j_{Cl,lipid}$ is bare lipid membranes' Cl^- mole flux, and σ_{PAH} is number of PAH[4] channels per unit membrane area.

Current-to-voltage measurement of PAH[4] reconstituted lipid membranes using DIB system.

A DIB setup was used to characterize the ionic transport properties of PAH[4] and PAP[5] channels (as a control) in lipid bilayer membranes. The lipid membranes were formed between two aqueous droplets anchored to wire-type electrodes in a transparent reservoir filled with oil, as described elsewhere[27,28]. In brief, the setup consisted of two lipid-encased aqueous droplets hanging from silver/silver chloride (Ag/AgCl) wires (Goodfellow) in oil (1:2 mixture of hexadecane (99%, Sigma) and decane (95%, Sigma). When the droplets were brought into contact, the lipid tails from each droplet interacted with each other at the interface to expel oil and form an oil-depleted hydrophobic center (i.e., a thinned lipid bilayer). To help the droplets anchor to Ag/AgCl wires, we coated their ball-ended tips with a 1% agarose gel solution. To confirm lipid bilayer formation, which is reflected as an increase in membrane capacitance, we supplied a 10 Hz, 10 mV triangular wave to the electrodes using a function generator (Hewlett-Packard 3314A). Due to the capacitive nature of the membrane, the resulting current response is square-like. As the area of the thinned lipid membrane grows, the peak-to-peak current amplitude increases until reaching a steady state. To generate the I-V relationships, we applied a 0.01 Hz, 50 mV sinusoidal voltage waveform and recorded the induced current. In parallel, to monitor the changes in the membrane we acquired images of the droplets from below through a 4X objective lens of an Olympus IX51 inverted microscope using a QI Click CCD. All current recordings were made using an Axopatch 200B patch clamp amplifier and Digidata 1440 data acquisition system (Molecular Devices). For all measurements, droplets and measurement probes were placed under a lab-made Faraday cage to minimize noise from the environment.

MD simulations.

All atom MD simulations were performed using the molecular dynamics program NAMD2[39]. Twenty five PAH[4] channels were arranged in a 5×5 array and embedded into a 14.4×14.4 nm^2 patch of a pre-equilibrated POPC lipid bilayer membrane. The lipid patch was generated from the CHARMM-GUI membrane builder[40] and equilibrated for approximately 400 ns. Lipid molecules overlapping with the channels were removed. The system was then solvated with the TIP3 water[41] using the Solvate plugin of VMD. Sodium and chloride ions were added using the Autoionize plugin of VMD to produced an electrically neutral solution of 0.6 M salt concentration. The resulting system measured $14.4 \times 14.4 \times 10$ nm^3 and contained approximately 170,000 atoms. Next, we created three conformations of PAH[4] dimers, namely lateral, orthogonal, and inverted, each comprised of two units of single PAH[4] channels (see Supplementary Information for details). We embedded 25 PAH[4] dimers in a regular 5×5 array into a 20×20 nm^2 patch of pre-equilibrated POPC lipid bilayer membrane. We solvated the structure and added ions to create a charge-neutral 0.6 M solution of NaCl in each system. The resulting system measured $20 \times 20 \times 10$ nm^3 and contained approximately 353,000 atoms. We created four such systems, three containing dimer arrays with different conformations and one where water molecules were placed inside an array of orthogonal PAH[4] dimers. Choosing the most conductive dimer conformation from these simulations, we created a pre-assembled cluster structures. Three different conformation of PAH[4] clusters were generated and embedded into a 14.4×14.4 nm^2 patch of pre-equilibrated POPC lipid bilayer membrane. Each structure was solvated by a 0.6 M NaCl solution. Each system measured $14.4 \times 14.4 \times 10$ nm^3 and contained approximately 172,000 atoms.

The assembled systems were subjected to energy minimization using the conjugate gradient method that removed steric clashes between the solute and solvent atoms. Following the energy minimization, the systems were subjected to short equilibration at constant number of atoms (N), constant pressure ($P = 1$ bar) and constant temperature ($T = 303$ K), i.e., an NPT ensemble with harmonic restraints to all the non-hydrogen atoms of PAH[4] channels with respect to their initial positions (with the spring constants of 1 kcal/mol Å^{-2}). Subsequently, the harmonic restraints were released completely, and the system was equilibrated free of any restraints.

The initial all-atom configuration of the AQP1 system was built starting from the all-atom structure of bovine AQP1, Protein Data Bank entry 1j4n[16]. The structure was embedded into a POPE lipid bilayer membrane as described in our previous study[42]. For the sake of comparison, the AQP1 system was simulated using the exactly same simulation protocols as the PAH[4] systems with 200 ns of simulation time.

All MD simulations were performed using periodic boundary conditions and particle mesh Ewald (PME) method to calculate the long range electrostatic interactions in NAMD2[39]. The Nose-Hoover Langevin piston[43,44] and Langevin thermostat were used to maintain the constant pressure and temperature in the system[45]. CHARMM36 force field parameters[46,47] described the bonded and non-bonded interactions of among PAH[4] channels, lipid bilayer membranes, water and ions along with NBFIX corrections for non-bonded interaction[48–51]. A 8-10-12 Å cutoff scheme was used to calculate van der Waals and short range

electrostatics forces. All simulations were performed using 1 femtosecond time steps for integrating the equation of motion. SETTLE algorithm[52] was applied to keep water molecules rigid whereas RATTLE algorithm[53] constrained all other covalent bonds involving hydrogen atoms. 300 – 400 ns equilibrium MD simulations were performed for each system which give rise to transmembrane water permeation through irregular dendritic paths in between the PAH[4] structures. The coordinates of the system were saved at the interval of 4.8 ps simulation. The analysis and post processing the simulation trajectories were performed using VMD and CPPTRAJ[54,55].

Supplementary Material

Refer to Web version on PubMed Central for supplementary material.

Acknowledgements

## References

1. Preston GM, Carroll TP, Guggino WB & Agre P Appearance of Water Channels in Xenopus Oocytes Expressing Red Cell CHIP28 Protein. Science 256, 385–387 (1992). [PubMed: 1373524]

2. Noda Y, Sohara E, Ohta E & Sasaki S Aquaporins in kidney pathophysiology. Nat. Rev. Nephrol 6, 168 (2010). [PubMed: 20101255]

3. Park HB, Kamcev J, Robeson LM, Elimelech M & Freeman BD Maximizing the right stuff: The trade-off between membrane permeability and selectivity. Science 356, eaab0530 (2017). [PubMed: 28619885]

4. Werber JR, Osuji CO & Elimelech M Materials for next-generation desalination and water purification membranes. Nat. Rev. Mater 1, 16018 (2016).

5. Shen Y. x., Saboe PO, Sines IT, Erbakan M & Kumar M Biomimetic membranes: A review. J. Membr. Sci 454, 359–381 (2014).

6. Hélix-Nielsen C Biomimetic Membranes as a Technology Platform: Challenges and Opportunities. Membranes 8, 44 (2018).

7. Song W, Lang C, Shen Y. x. & Kumar M Design Considerations for Artificial Water Channel–Based Membranes. Ann. Rev. Mater. Res 48, 57–82 (2018).

8. Song W, Tu Y-M, Oh H, Samineni L & Kumar M Hierarchical Optimization of High-Performance Biomimetic and Bioinspired Membranes. Langmuir 35, 589–607 (2019). [PubMed: 30577695]

9. Horner A et al. The mobility of single-file water molecules is governed by the number of H-bonds they may form with channel-lining residues. Sci. Adv 1, e1400083 (2015). [PubMed: 26167541]

10. Shen Y. x. et al. Achieving high permeability and enhanced selectivity for Angstrom-scale separations using artificial water channel membranes. Nat. Commun 9, 2294 (2018). [PubMed: 29895901]

11. Licsandru E et al. Salt-Excluding Artificial Water Channels Exhibiting Enhanced Dipolar Water and Proton Translocation. J. Am. Chem. Soc 138, 5403–5409 (2016). [PubMed: 27063409]

12. Shen Y. x. et al. Highly permeable artificial water channels that can self-assemble into two-dimensional arrays. Proc. Natl. Acad. Sci. USA 112, 9810–9815 (2015). [PubMed: 26216964]

13. Tunuguntla RH et al. Enhanced water permeability and tunable ion selectivity in subnanometer carbon nanotube porins. Science 357, 792–796 (2017). [PubMed: 28839070]

14. Freger V Selectivity and polarization in water channel membranes: lessons learned from polymeric membranes and CNTs. Faraday Discuss. 209, 371–388 (2018). [PubMed: 29972390]

15. Song W & Kumar M Artificial water channels: toward and beyond desalination. Curr. Opin. Chem. Eng 25, 9–17 (2019).

16. Sui H, Han B-G, Lee JK, Walian P & Jap BK Structural basis of water-specific transport through the AQP1 water channel. Nature 414, 872–878 (2001). [PubMed: 11780053]

17. Tajkhorshid E et al. Control of the Selectivity of the Aquaporin Water Channel Family by Global Orientational Tuning. Science 296, 525–530 (2002). [PubMed: 11964478]

18. Saparov SM et al. Mobility of a One-Dimensional Confined File of Water Molecules as a Function of File Length. Phys. Rev. Lett 96, 148101 (2006). [PubMed: 16712124]

19. Hannesschläger C, Barta T, Siligan C & Horner A Quantification of Water Flux in Vesicular Systems. Sci. Rep 8, 8516 (2018). [PubMed: 29867158]

20. Borgnia MJ, Kozono D, Calamita G, Maloney PC & Agre P Functional reconstitution and characterization of AqpZ, the E. coli water channel protein11Edited by W. Baumeister. J. Mol. Biol 291, 1169–1179 (1999). [PubMed: 10518952]

21. Pohl P, Saparov SM, Borgnia MJ & Agre P Highly selective water channel activity measured by voltage clamp: Analysis of planar lipid bilayers reconstituted with purified AqpZ. Proc. Natl. Acad. Sci. USA 98, 9624–9629 (2001). [PubMed: 11493683]

22. Horner A & Pohl P Comment on "Enhanced water permeability and tunable ion selectivity in subnanometer carbon nanotube porins". Science 359, eaap9173 (2018). [PubMed: 29599215]

23. Baaden M et al. Biomimetic water channels: general discussion. Faraday Discuss. 209, 205–229 (2018). [PubMed: 30225508]

24. Geise GM, Park HB, Sagle AC, Freeman BD & McGrath JE Water permeability and water/salt selectivity tradeoff in polymers for desalination. J. Membr. Sci 369, 130–138 (2011).

25. Toyoshima Y & Thompson TE Chloride flux in bilayer membranes. Chloride permeability in aqueous dispersions of single-walled, bilayer vesicles. Biochemistry 14, 1525–1531 (1975). [PubMed: 235955]

26. Lang C et al. Biomimetic Transmembrane Channels with High Stability and Transporting Efficiency from Helically Folded Macromolecules. Angew. Chem. Int. Ed 55, 9723–9727 (2016).

27. Taylor GJ, Venkatesan GA, Collier CP & Sarles SA Direct in situ measurement of specific capacitance, monolayer tension, and bilayer tension in a droplet interface bilayer. Soft Matter 11, 7592–7605 (2015). [PubMed: 26289743]

28. Najem JS et al. Memristive Ion Channel-Doped Biomembranes as Synaptic Mimics. ACS Nano 12, 4702–4711 (2018). [PubMed: 29578693]

29. Venkatesan GA et al. Adsorption Kinetics Dictate Monolayer Self-Assembly for Both Lipid-In and Lipid-Out Approaches to Droplet Interface Bilayer Formation. Langmuir 31, 12883–12893 (2015). [PubMed: 26556227]

30. Taylor GJ & Sarles SA Heating-Enabled Formation of Droplet Interface Bilayers Using Escherichia coli Total Lipid Extract. Langmuir 31, 325–337 (2015). [PubMed: 25514167]

31. Najem JS et al. Dynamical nonlinear memory capacitance in biomimetic membranes. Nat. Commun 10, 3239 (2019). [PubMed: 31324794]

32. Werber JR & Elimelech M Permselectivity limits of biomimetic desalination membranes. Sci. Adv 4, eaar8266 (2018). [PubMed: 29963628]

33. Erbakan M et al. Molecular Cloning, Overexpression and Characterization of a Novel Water Channel Protein from Rhodobacter sphaeroides. PLoS One 9, e86830 (2014). [PubMed: 24497982]

34. Horner A & Pohl P Single-file transport of water through membrane channels. Faraday Discuss. 209, 9–33 (2018). [PubMed: 30014085]

35. Woodle MC & Papahadjopoulos D [9] Liposome preparation and size characterization. Methods Enzymol. 171, 193–217 (1989). [PubMed: 2593841]

36. Latimer P & Pyle BE Light Scattering at Various Angles: Theoretical Predictions of the Effects of Particle Volume Changes. Biophys. J 12, 764–773 (1972). [PubMed: 4556610]

37. Tong J, Canty JT, Briggs MM & McIntosh TJ The water permeability of lens aquaporin-0 depends on its lipid bilayer environment. Exp. Eye Res 113, 32–40 (2013). [PubMed: 23680159]

38. Biwersi J, Tulk B & Verkman AS Long-Wavelength Chloride-Sensitive Fluorescent Indicators. Anal. Biochem 219, 139–143 (1994). [PubMed: 8059940]

39. Phillips JC et al. Scalable molecular dynamics with NAMD. J. Comput. Chem 26, 1781–1802 (2005). [PubMed: 16222654]

40. Jo S, Kim T, Iyer VG & Im W CHARMM-GUI: a web-based graphical user interface for CHARMM. J. Comput. Chem 29, 1859–1865 (2008). [PubMed: 18351591]

41. Jorgensen WL, Chandrasekhar J, Madura JD, Impey RW & Klein ML Comparison of simple potential function for simulating liquid water. J. Chem. Phys 79, 926–935 (1983).

42. Decker K et al. Selective Permeability of Truncated Aquaporin 1 in Silico. ACS Biomater. Sci. Eng 3, 342–348 (2017).

43. Feller SE, Zhang Y, Pastor RW & Brooks BR Constant pressure molecular dynamics simulation: the Langevin piston method. J. Chem. Phys 103, 4613–4621 (1995).

44. Martyna GJ, Tobias DJ & Klein ML Constant pressure molecular dynamics algorithms. J. Chem. Phys 101, 4177–4189 (1994).

45. Sindhikara DJ, Kim S, Voter AF & Roitberg AE Bad seeds sprout perilous dynamics: Stochastic thermostat induced trajectory synchronization in biomolecules. J. Chem. Theory Comput 5, 1624–1631 (2009). [PubMed: 26609854]

46. Best RB et al. Optimization of the additive CHARMM all-atom protein force field targeting improved sampling of the backbone ϕ, ψ and side-chain $\chi 1$ and $\chi 2$ dihedral angles. J. Chem. Theory Comput 8, 3257–3273 (2012). [PubMed: 23341755]

47. Klauda JB et al. Update of the CHARMM all-atom additive force field for lipids: validation on six lipid types. J. Phys. Chem. B 114, 7830–7843 (2010). [PubMed: 20496934]

48. Yoo J & Aksimentiev A New tricks for old dogs: improving the accuracy of biomolecular force fields by pair-specific corrections to non-bonded interactions. Phys. Chem. Chem. Phys 20, 8432–8449 (2018). [PubMed: 29547221]

49. Yoo J & Aksimentiev A Refined Parameterization of Nonbonded Interactions Improves Conformational Sampling and Kinetics of Protein Folding Simulations. J. Phys. Chem. Lett 7, 3812–3818 (2016). [PubMed: 27617340]

50. Yoo J & Aksimentiev A Improved parameterization of amine–carboxylate and amine–phosphate interactions for molecular dynamics simulations using the CHARMM and AMBER force fields. J. Chem. Theory Comput 12, 430–443 (2015). [PubMed: 26632962]

51. Yoo J & Aksimentiev A Improved parametrization of Li+, Na+, K+, and Mg2+ ions for all-atom molecular dynamics simulations of nucleic acid systems. J. Phys. Chem. Lett 3, 45–50 (2012).

52. Miyamoto S & Kollman PA Settle: An analytical version of the SHAKE and RATTLE algorithm for rigid water models. J. Comput. Chem 13, 952–962 (1992).

53. Andersen HC Rattle: A "velocity" version of the shake algorithm for molecular dynamics calculations. J. Comput. Phys 52, 24–34 (1983).

54. Humphrey W, Dalke A & Schulten K VMD: Visual molecular dynamics. J. Mol. Graphics Model 14, 33–38 (1996).

55. Roe DR & Cheatham TE III. PTRAJ and CPPTRAJ: Software for Processing and Analysis of Molecular Dynamics Trajectory Data. J. Chem. Theory Comput 9, 3084–3095 (2013). [PubMed: 26583988]
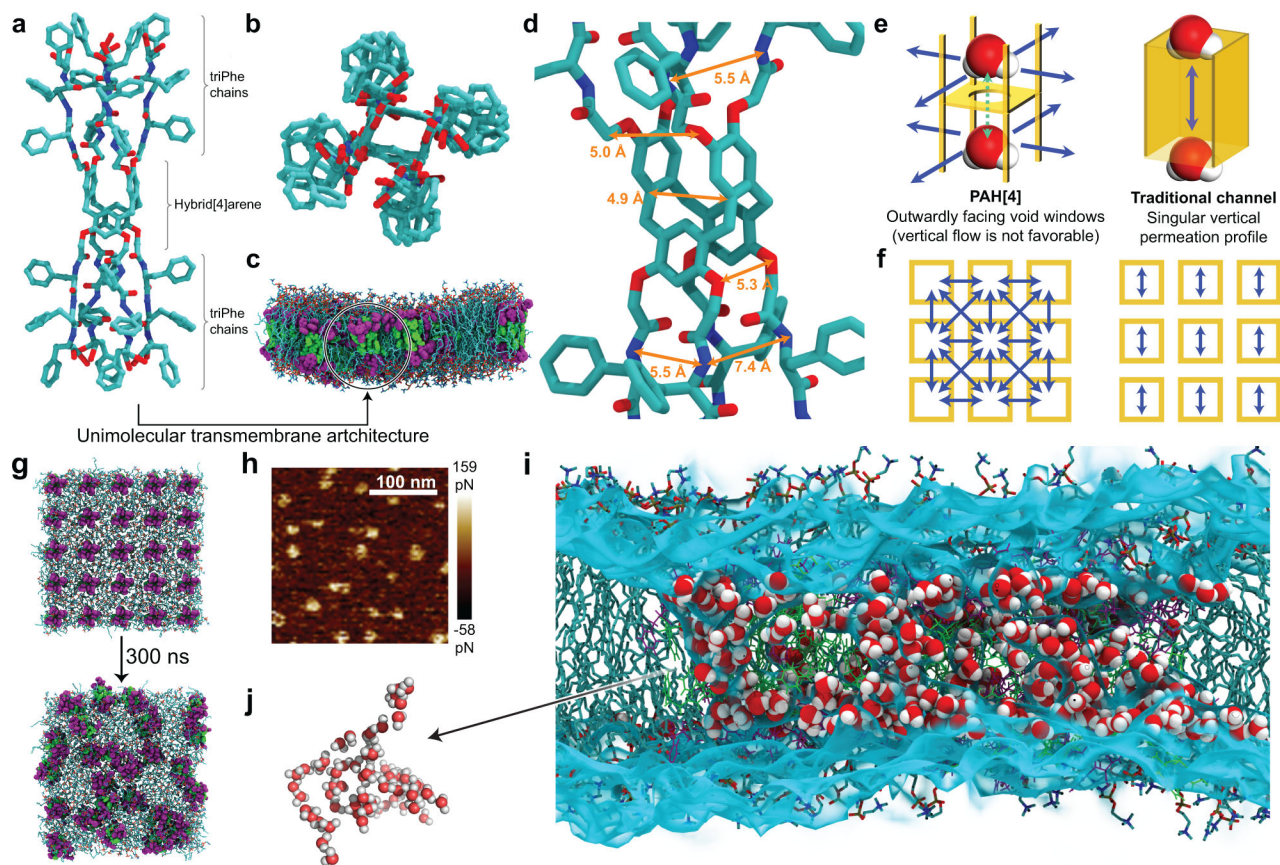
Fig. 1. Cluster-forming PAH[4] channels.

a,b, Side (**a**) and top (**b**) views of molecular models of PAH[4] indicate cylinder-like transmembrane structures. **c**, MD simulation snapshots of PAH[4]s spanning lipid bilayer membranes. **d**, Tilted top view of energy-minimized PAH[4] structure shows outwardly facing void windows. **e,f**, Schematic comparison of proposed water permeation paths (blue arrows) between PAH[4] and traditional channel configurations (**e**) and paths through nine channel aggregates (yellow boxes) seen from top view (**f**), respectively. **g**, Snapshots from an MD simulation showing lateral aggregation of PAH[4]s in lipid bilayer membrane patches. **h**, AFM image (adhesion force) of PAH[4]-reconstituted supported lipid membranes shows aggregated domains of PAH[4] channels. **i**, Cross-sectional MD simulation snapshot of water permeation through PAH[4] cluster embedded in lipid bilayer patch, showing multiple water wires. **j**, A single illustrative water-wire network (of many) connecting the water compartments across the membrane. In the MD simulation panels, molecules are represented by the following colors; PAH[4] (purple and green), lipid (turquoise), and water (red and white).
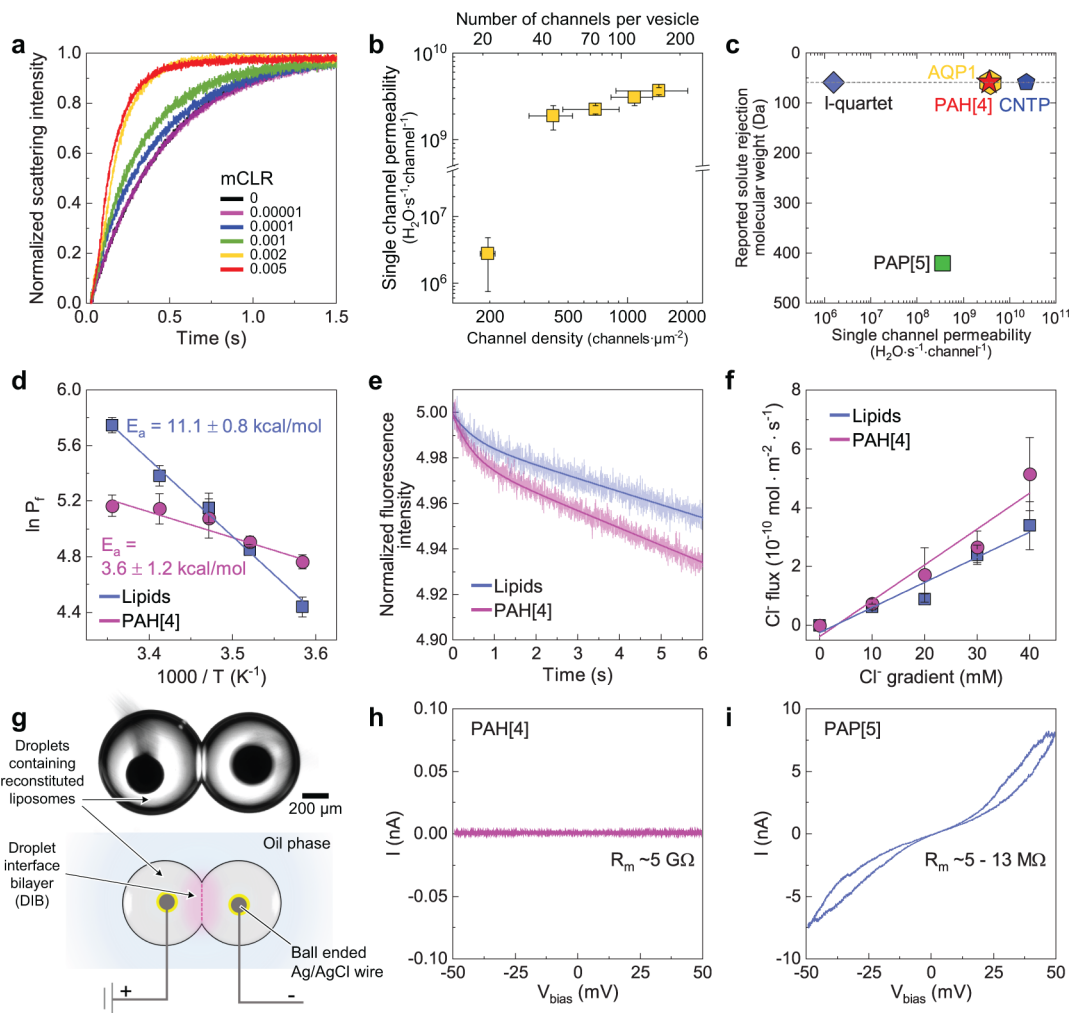
Fig. 2. Measurements of water and ion conduction rates through PAH[4]s.
a, Stopped-flow light scattering traces of PAH[4] reconstituted PC/PS vesicles with different mCLRs under inwardly directed osmotic gradient indicate increasing permeability with increased channel concentrations (molar ratio of channels to lipids, mCLRs). **b**, Single PAH[4] channel permeability measured at different channel densities indicates a jump in permeability when channel concentrations reach a threshold between ~ 200 channels·μm^{-2} (or ~20 channels per average sized vesicle) and ~420 channels·μm^{-2} (or ~45 channels/ vesicle) indicating possible cooperativity. **c**, Comparison of calculated single channel permeability and reported effective solute rejection property of representative AWCs (imidazole-quartet and peptide-appended pillar[5]arene, I-quartet and PAP[5], respectively), AQP1, and CNTPs. **d**, Arrhenius plots of bare lipid membrane permeability (P$_f$, μm/s) and PAH[4]-mediated membrane permeability. **e**, Comparison of fluorescence intensity traces between lucigenin encapsulating control lipid and PAH[4]-reconstituted vesicles (mCLR 0.005), measured at 20 mM Cl$^-$ concentration gradient. **f**, Plots of Cl$^-$ flux as a function of Cl$^-$ concentration (mM) gradients for both control and PAH[4]-reconstituted lipid membranes. **g**, Optical microscope image of hanging droplets with DIB at droplet-contacting interface (upper) and schematic illustration of ionic current measurement setup (bottom
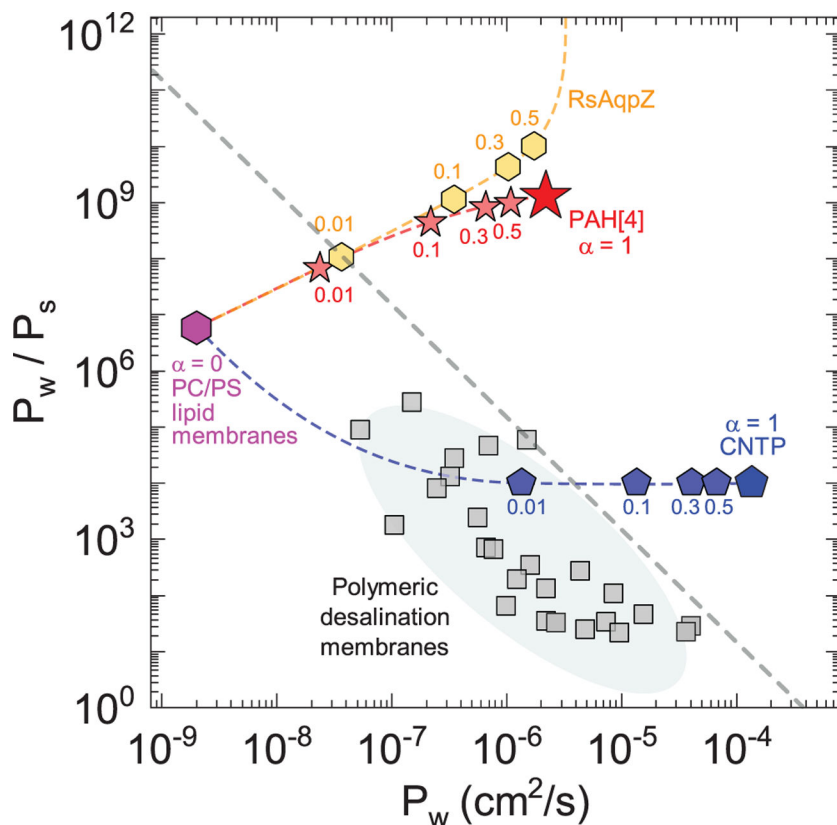
panel). **h,i**, I-V plots of PAH[4] (mCLR 0.005) (**h**) and PAP[5] (mCLR 0.002) (**i**) reconstituted membranes measured under the DIB system. The nonlinearity of I-V curves of PAP[5] membranes is caused by membrane area change due to electrowetting, not channels[28].

Fig. 3. Intrinsic water/NaCl selectivity (P_W/P_S) versus water permeability (P_W) of PAH[4], CNTP and RsAqpZ based biomimetic membranes.

Data points of channel-reconstituted biomimetic membranes with PC/PS matrix molecules with increasing fractional area of the membranes occupied by the channels ($\alpha = 0.5$ indicates 50% of membrane area is occupied by channels) are compared; α values indicate the corresponding data points for the PAH[4] (red stars), RsAqpZ (orange hexagons), and CNTP (blue pentagons) membranes, respectively. Dashed lines for channel-based membranes are guides for the eye. Data for representative polymeric desalination membranes (grey squares) and their upper bound tradeoff line (dashed gray line) are adapted from reference[24].
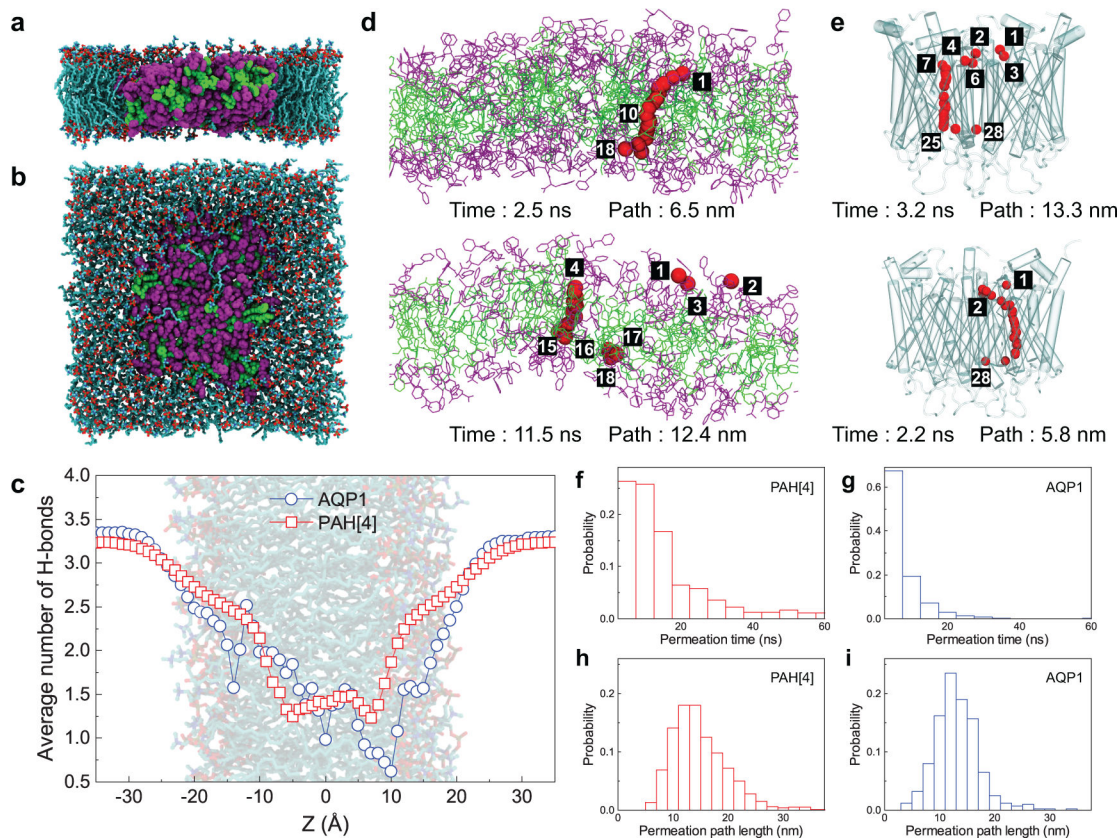
Fig. 4. MD simulations of a 22-mer cluster of PAH[4] channels and of a aquaporin-1 (AQP1) tetramer embedded in a lipid bilayer membrane.

a,b, Side (**a**) and top (**b**) views of a PAH[4] 22-mer cluster (purple and green) embedded in a lipid bilayer membrane (turquoise); water and ions are not shown for clarity. **c**, Average number of hydrogen bonds formed by a permeating water molecule as the function of its Z-coordinate in an AQP1 tetramer and a cluster of PAH[4] channels embedded in a lipid bilayer membrane. To calculate the number of H-bonds, a 3.5 Å distance cutoff between donor and acceptor and a 40° angle cutoff for donor-hydrogen-acceptor were used. The number of H-bonds was averaged over all permeated water molecules during the course of the MD trajectory (~800 and ~400 for PAH[4] and AQP1, respectively). **d,e**, The approximated path of the two representative water molecules permeated through the PAH[4] cluster (**d**) and the AQP1 tetramer (**e**). The PAH[4] molecules are shown using green and purple lines whereas the AQP1channel is shown using white semi-transparent cylinders. The red spheres show the average location of the permeating water molecule in each 1 Å bin along the Z direction during the permeation path. Lipid and other water molecules are not shown for clarity. The numbers specify the bin index along the Z axis, from 1 to 18 or 1 to 28 bins for PAH[4] and AQP1, respectively; some bin numbers are omitted for clarity. The permeation path length and the permeation time of the respective water molecules are specified in each figure. **f,g**, The normalized distribution of the permeation time for all water molecules that passed through the PAH[4] cluster (**f**) and the AQP1 tetramer (**g**). **h,i**, The

normalized distribution of the permeation length for all water molecules the passed through the PAH[4] cluster (**h**) and the AQP1tetramer (**i**).